

# Auxiliary Power Module Elimination in EVs Using Dual Inverter Drivetrain

Caniggia Castro Diniz Viana , *Student Member, IEEE*, Mehanathan Pathmanathan , *Senior Member, IEEE*, and Peter W. Lehn, *Senior Member, IEEE*

**Abstract**—As electric vehicles compete with internal combustion engine cars, cost and weight savings remain central research objectives. The auxiliary power module, a dc/dc converter responsible for stepping down the power from the main traction battery to the auxiliary battery, has gained attention as a component where weight and cost savings can be achieved. With the auxiliary power module responsible for feeding everything from headlights to rising vehicular computational demands, these savings become evermore significant. This article introduces a system that integrates traction-to-auxiliary power conversion into the dual inverter drivetrain, leveraging typically underutilized degrees of freedom in the drive inverter to implement and control the dc/dc conversion eliminating the auxiliary power module. Due to the high level of integration, the proposed solution improves on existing literature by exclusively using the drivetrain's active switches. Beyond capital savings and simplicity, this ensures no additional switching losses compared to regular driving operation. A mathematical model is motivated analytically and validated using computational simulations. A 1.2 kW prototype is constructed to validate the introduced concept experimentally.

**Index Terms**—Auxiliary power module (APM), electric vehicle (EV) drivetrain, integrated, modeling and control, traction to auxiliary (T2A) charger.

## I. INTRODUCTION

RECENT developments in power processing and energy storage have the potential to decrease electric vehicle (EV) production cost and weight, with the latter being a determining factor of vehicle range [1]. The range and cost of EVs, compared to ICE vehicles, remain two prominent barriers limiting the pace of EV adoption [2].

Adding to price and weight concerns is the increasing auxiliary load power consumption trend. Modern car consumers expect high-end connectivity, comfort, and computational power. To provide these features, an auxiliary power module (APM) is included and responsible for traction-to-auxiliary (T2A) energy conversion. The power requirements from the APM are

Manuscript received November 29, 2021; revised March 29, 2022; accepted May 15, 2022. Date of publication May 20, 2022; date of current version June 24, 2022. This work was supported by the Natural Sciences and Engineering Research Council of Canada (NSERC) under Grant CRDPJ 513206-17. Recommended for publication by Associate Editor R. Zane. (*Corresponding author: Caniggia Castro Diniz Viana.*)

The authors are with the Department of Electrical and Computing Engineering, University of Toronto, Toronto, ON M5S 3G4, Canada (e-mail: caniggia-diniz@gmail.com; meha.pathmanathan@utoronto.ca; lehn@ecf.utoronto.ca).

Color versions of one or more figures in this article are available at <https://doi.org/10.1109/TPEL.2022.3176240>.

Digital Object Identifier 10.1109/TPEL.2022.3176240

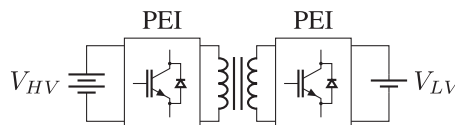


Fig. 1. Dedicated dual active bridge APM charger.

often around 2.5 kW [3], with industry and academia recently investigating 6 kW power levels [4]–[6]. This power is needed to supply loads such as headlights, onboard computing systems, air conditioning, and many other subsystems. Consequently, EV's APM solutions are growing in cost and weight, partially undermining the weight savings resulting from the advancements in drivetrain power conversion technology.

The classical APM implementation includes a dedicated isolated dc/dc converter from the high voltage (HV) battery to the low voltage (LV) battery. In [7] and [8], several isolated dc/dc topologies and their suitability are investigated, considering different primary and secondary side power electronic interfaces (PEIs). The solution proposed in [9], for instance, includes a dual active bridge (DAB) for T2A conversion, as shown in Fig. 1.

Recent research effort has been dedicated to reducing the size of the APM, given its increasing relevance. Two prominent strategies employed to meet this goal are higher switching frequency and converter integration.

A higher switching frequency leads to significantly reduced mass and cost of passive filtering components. In [10], an APM converter is designed using GaN switches with 700 kHz switching frequency. Several other authors also achieve high power density by leveraging the high frequencies enabled by wide-bandgap devices [11]. However, high switching frequencies may lead to more expensive switches, complex gate-driver design, and increased switching losses.

Converter integration, in this context, is characterized by the repurposing of components previously present in the vehicle to implement, partially or entirely, the APM. These previously present components may be, for instance, included for driving or charging purposes, irrespective of the APM. In [12], a topology is explored where a half-bridge is shared between the onboard charger (OBC) converter and the DAB converter implementing the APM. As a result, the solution in [12] reduces the number of half-bridges in the system by one.

Some solutions attempt to integrate additional functionality into the APM. In [13]–[15], the APM is integrated with active power decoupling (APD) functionality. The APD system

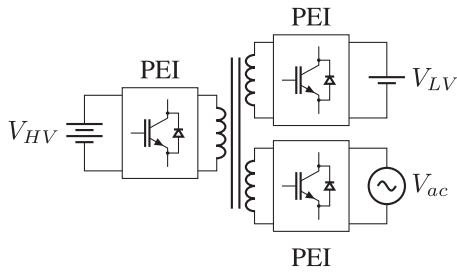


Fig. 2. Multiport ac charging system with T2A capability with shared transformer and PEI proposed in [21].

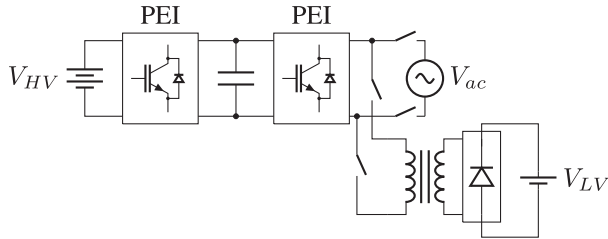


Fig. 3. Multiport ac charging system with T2A capability and shared PEI proposed in [24].

diverges the second harmonic power ripple from the OBC single-phase input to an auxiliary capacitor, thereby reducing or eliminating the second harmonic power ripple into the traction battery. In other implementations, the APM is integrated with HV battery balancing, with the T2A conversion being fed from different cells of the traction battery [16]–[19].

A clear trend to integrate OBC and APM has been reported in the literature [20], with two main approaches being employed. The first approach consists of leveraging the isolation transformer of the OBC, with an additional winding set and PEI included to implement the APM. The approaches used in [21] and [22], for example, add an APM port to the OBC, effectively generating a multiport converter, such as that shown in Fig. 2. As explored in [23], additional ports can be included for additional functionality, such as onboard photovoltaic generation.

Another approach to integrating the OBC and APM circuits is to employ a bidirectional OBC that, while idle, can be used as the primary stage of the APM. The solutions introduced in [24] and [25] explore this strategy. The resulting system is as shown in Fig. 3. These systems can implement the APM with remarkable cost-effectiveness, as the additional circuitry needed is minimal and potentially entirely passive [24]. Nonetheless, while in T2A operation, the system incurs all of the losses associated with the OBC. Moreover, on this kind of implementation, the system cannot operate while the OBC charger is used to charge the HV battery, which may be an extended period for level 1 charging.

Integrated charging and drivetrain solutions have been proposed where the OBC does not include an isolation stage and has reduced or no PEI dedicated exclusively for charging operation [26], [27], in particular for the dual inverter drivetrain. The dual inverter drivetrain boasts some valuable advantages for EV applications, including redundancy and fault resiliency

[28]–[30], suitability for a wide speed range of operation [31], and low current distortion [32], [33], while having the same total semiconductor apparent power rating as a comparable single inverter.

The solutions proposed in [26] and [27] significantly reduce the vehicle's mass but do not allow for the implementation of multiport OBC integrated APMs, as in [21] and [22], or using the OBC as a front-end, as in [24] and [25]. For such systems, solutions are yet to be proposed to integrate the APM into existing modules. One module that rises as a potential candidate for APM integration is the drivetrain itself. EV drivetrains typically have an underutilized degree of freedom, the neutral current, or zero-axis/zero-sequence. Previous work has been proposed leveraging this degree of freedom to implement other functionalities, such as dc fast charging [34], even during driving operation [35].

This work presents a fully integrated T2A supply topology for dual inverter drivetrain systems, leveraging and controlling the switching frequency component of the zero-sequence current through the machine to perform T2A power transfer. The proposed circuit possesses the following set of unique features in comparison to solutions previously discussed in the literature.

- 1) The system can be implemented on a dual-inverter drivetrain without adding active switches, thereby providing a cost-effective and straightforward way to add the T2A functionality. The added circuitry includes only a compensation capacitor, an isolation transformer, a diode rectifier, and an optional output CL low-pass filter, drastically reducing the T2A system's deployment cost.
- 2) The system does not require any specific OBC system, thereby providing a flexible T2A integration for dual inverter systems.
- 3) The system does not require any additional switching action compared to regular driving operation, resulting in no additional switching loss. This feature is expected to increase the total vehicle range compared to a dedicated APM.
- 4) A control algorithm that leverages additional degrees of freedom of the dual inverter to fully control T2A charging power without disturbing torque production using the zero-axis voltage. This allows for the seamless operation of the T2A system while driving or at a standstill.

## II. PROPOSED TOPOLOGY

The proposed topology is based on the dual inverter drivetrain, discussed in [26] and [27], and is implemented by connecting the primary side of a transformer and a compensation capacitor to the dual inverter, with the secondary side of the transformer connected to a rectifier, followed by an optional CL filter and the auxiliary LV battery. The series combination of compensation capacitor and the primary side of the transformers are connected to the negative terminal of each battery. The high-level view of the proposed system is shown in Fig. 4.

Observing the circuit shown in Fig. 4, it can be noted that the current into the primary side of the transformer equals the sum of the three motor windings currents,  $i_a$ ,  $i_b$ , and  $i_c$ ,

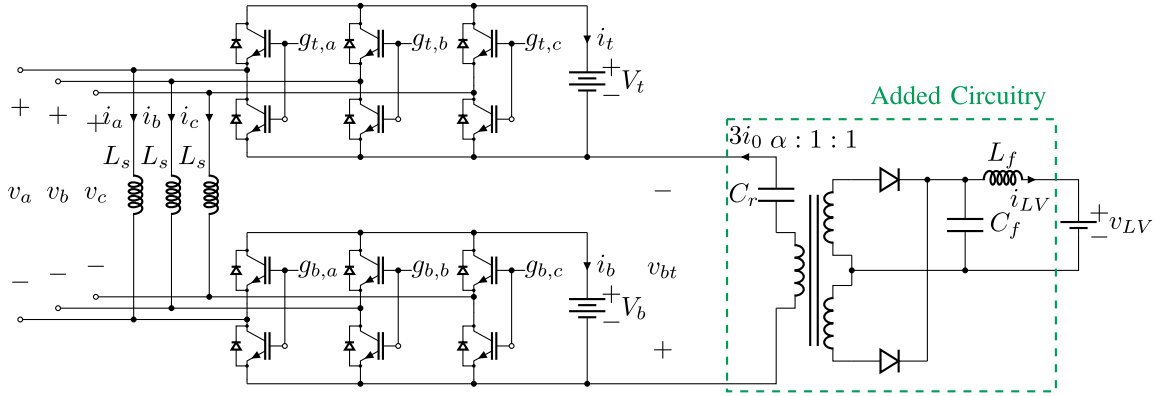


Fig. 4. Proposed circuitry addition to the drivetrain for T2A operation.

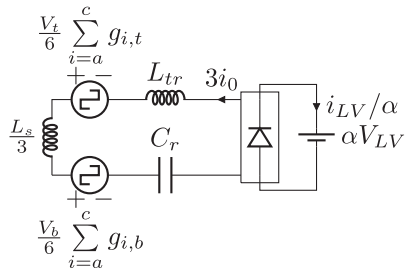


Fig. 5. Simplified zero-axis equivalent model of the proposed system.

termed the common-mode current in [36]. The common-mode equivalent of the circuit of Fig. 4 is derived as prescribed in [36]. This transformation computes the Thevenin equivalent of the system as seen by the zero-axis, as defined in [37] and [38]. The resulting equivalent circuit is shown in Fig. 5 and simplifies the proposed system. It is also apparent that the common-mode current is triple the zero-axis current, following the definitions in [37] and [38]. The Clarke transformation, as discussed in [38], will be leveraged throughout the following derivations. In these derivations, the optional low-pass filter effects are neglected for simplicity.

In this context, we have the following.

- 1)  $i_0$  is the instantaneous average current amongst the three-phase windings, defined as  $i_0 = \frac{1}{3}(i_a + i_b + i_c)$ .
- 2)  $L_s$  is the motor's stator winding phase leakage inductance.
- 3)  $V_t$  is the top battery voltage.
- 4)  $V_b$  is the bottom battery voltage.
- 5)  $C_r$  is the compensation capacitor, included to cancel the combined inductive reactance of the transformer and the zero-sequence inductance of the motor.
- 6)  $L_{tr}$  is the leakage inductance of the step-down transformer, referred to as the primary (HV) side.
- 7)  $g_{i,t}$  is the gating state of the phase  $i$ ,  $i \in \{a, b, c\}$ , of the top inverter; defined to be 1 when the top switch of the associated half-bridge is ON and  $-1$  when the bottom switch is ON.
- 8)  $g_{i,b}$  is the gating state of the phase  $i$ ,  $i \in \{a, b, c\}$ , of the bottom inverter; defined to be 1 when the top switch of

the associated half-bridge is ON and  $-1$  when the bottom switch is ON.

- 9)  $\alpha$  is the transformer's turns ratio, as shown in Fig. 4.

#### A. Operating Principle

The equivalent zero-axis voltage produced by the dual inverter

$$v_0 = \frac{1}{3}(v_a + v_b + v_c) + v_{bt} \quad (1)$$

represents the average voltage applied by the dual inverter to the series combination of motor winding leakage inductance and additional circuitry, as defined by the standard Clarke transformation [38]. This voltage can be defined in terms of the instantaneous gating signals and the battery voltages as

$$v_0 = \frac{V_t}{6} \sum_{i=a}^c g_{i,t} - \frac{V_b}{6} \sum_{i=a}^c g_{i,b} \quad (2)$$

and can be controlled to track the desired zero-axis current  $i_0^*$ , consequently controlling the current into the T2A transformer.

Although the system can be operated with different energy storage voltages for each inverter, the energy storage voltages are assumed to be equal in the following derivations for clarity and succinctness. Under this assumption, the voltage of both energy storage units, e.g., batteries, is defined as

$$V_{bat} \triangleq V_t = V_b \quad (3)$$

such that the total voltage  $v_0$ , driving the circuit shown in Fig. 5, can be rewritten as

$$v_0 = \frac{V_{bat}}{6} \sum_{i=a}^c (g_{i,t} - g_{i,b}). \quad (4)$$

To facilitate power transfer at the switching frequency, the included capacitance  $C_r$  and transformer leakage inductance  $L_{tr}$  are designed to resonate at the switching frequency, ensuring minimum loop impedance. Hence

$$C_r = \frac{1}{(2\pi f_{sw})^2 \left( \frac{L_s}{3} + L_{tr} \right)}. \quad (5)$$

In this approach, the magnetizing inductive reactance of the transformer, as seen by the primary side, is designed to be large

and is neglected for compensation purposes. The resonance from (5) allows the fundamental zero-axis voltage harmonics produced by switching the main traction inverters at the switching frequency to generate a significant current through the loop, thereby facilitating T2A power transfer. The resonant operation of the system ensures that higher order harmonics of the switching frequency do not generate significant currents.

Fourier analysis can be used to determine the frequency components of the zero-axis voltage,  $v_0$  over the switching period, from

$$\underline{V}_0^{(n)} = \frac{2}{T_{sw}} \int_{-\frac{T_{sw}}{2}}^{\frac{T_{sw}}{2}} v_0 e^{-j2\pi n f_{sw} t} dt \quad (6)$$

where

- 1)  $\underline{V}_0^{(n)}$  denotes peak phasor voltage at the  $n$ th harmonic of the switching frequency  $f_{sw}$ ;
- 2)  $T_{sw}$  is the fundamental period associated with  $f_{sw}$ .

To control the power transfer in the circuit shown in Fig. 4, the magnitude of the fundamental harmonic voltage phasor,  $|\underline{V}_0^{(1)}|$ , needs to be controlled. Given the relation shown in (4), it is necessary to know the gating pulse sequencing in order to solve (6), as

$$\underline{V}_0^{(1)} = \frac{V_{bat}}{3T_{sw}} \int_{-\frac{T_{sw}}{2}}^{\frac{T_{sw}}{2}} \left( \sum_{i=a}^c (g_{i,t} - g_{i,b}) \right) e^{-j2\pi f_{sw} t} dt. \quad (7)$$

A suitable gating pulse generation, which allows for T2A control while not interfering with the drive control, is discussed below.

### B. Magnitude of Switching Frequency Component of Zero-Sequence Voltage

Assuming, without loss of generality, that the modulation technique used to drive the electric motor is sinusoidal pulsewidth modulation (PWM), a phase shift  $\delta$  is introduced between the triangular carriers used to generate the gating pulses of the top and bottom inverters to control  $|\underline{V}_0^{(1)}|$ . This phase shift is implemented with a delay of  $\Delta t$  between carriers of the top and bottom inverters, i.e.,

$$\delta = \left( \frac{\Delta t}{T_{sw}} \right) 2\pi. \quad (8)$$

The system is envisioned to operate during both driving and standstill conditions. When driving, a control system produces a reference voltage suitable for torque production in the motor. This voltage defines a set of modulating signals,  $m_a$ ,  $m_b$ , and  $m_c$ . The modulating signals can be written in space-vector form through the use of the Park transformation. The modulation vector is defined by

$$\vec{m} = m_d + jm_q = M e^{j\theta} \quad (9)$$

where we have the following.

- 1)  $M$  is the modulation index or, equivalently, the amplitude of the modulation vector, typically related to the speed of the car.  $M$  is approximately 0 when the car is at standstill.

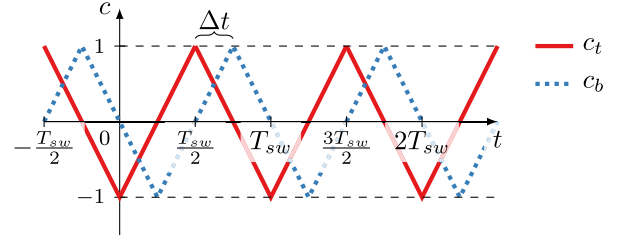


Fig. 6. PWM carrier visual definition and top-to-bottom phase-shift representation.

- 2)  $\theta$  is the angle of  $\vec{m}$ , which is dependent on the angle of the voltage space-vector, requested by the driving control system.

The modulating signals used to generate each phase's gating pulses are defined by

$$\begin{bmatrix} m_a \\ m_b \\ m_c \end{bmatrix} = \begin{bmatrix} M \cos(\theta) \\ M \cos\left(\theta - \frac{2\pi}{3}\right) \\ M \cos\left(\theta + \frac{2\pi}{3}\right) \end{bmatrix}. \quad (10)$$

The gating pulses  $g_{i,t}$  and  $g_{i,b}$  can, therefore, be generated by comparing the modulating signals with the top and bottom inverter carrier signals,  $c_t$  and  $c_b$ , respectively

$$\begin{bmatrix} g_{a,t} \\ g_{b,t} \\ g_{c,t} \end{bmatrix} = \text{sign} \left( \begin{bmatrix} m_a \\ m_b \\ m_c \end{bmatrix} - c_t \right) \quad (11)$$

and

$$\begin{bmatrix} g_{a,b} \\ g_{b,b} \\ g_{c,b} \end{bmatrix} = \text{sign} \left( - \begin{bmatrix} m_a \\ m_b \\ m_c \end{bmatrix} - c_b \right) \quad (12)$$

where we have the following.

- 1)  $c_t$  is a triangular carrier signal of the top inverter, with frequency  $f_{sw}$ , ranging between  $-1$  and  $1$ , as illustrated in Fig. 6.
- 2)  $c_b$  is a delayed version of  $c_t$ , which is used to generate the gating pulses of the bottom inverter, i.e.,

$$c_b(t) = c_t(t - \Delta t) \quad (13)$$

where

$$0 \leq \Delta t \leq \frac{T_{sw}}{2}. \quad (14)$$

Once the gating pulses are defined, based on the choice of carrier and modulating signals, (7) can be solved in light of (8), and (10)–(13), and assuming the modulating signals vary much slower than the carrier signals. The result, describing magnitude of the fundamental frequency component of  $v_0$ , can be written as a function of the modulation index  $M$  modulation angle  $\theta$  and the carrier phase-shift  $\delta$

$$\begin{aligned} |\underline{V}_0^{(1)}| &= \\ \frac{4V_{bat}}{3\pi} &\left[ \sum_{i=-1}^1 \cos\left(\frac{M\pi}{2} \cos\left(\theta + i\frac{2\pi}{3}\right)\right) \right] \left| \sin\left(\frac{\delta}{2}\right) \right|. \end{aligned} \quad (15)$$

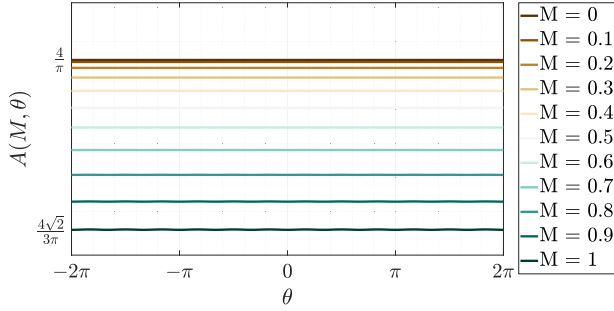


Fig. 7. Weak dependence of maximum applicable voltage, in p.u.,  $A(M, \theta)$ , on the modulation angle.

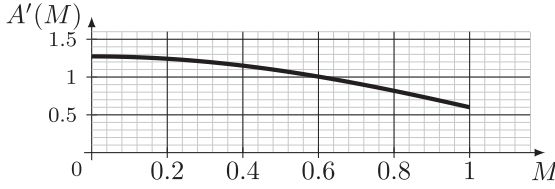


Fig. 8. Maximum applicable voltage in per-unit.

The maximum attainable amplitude of  $|\underline{V}_0^{(1)}|$ , enacted when  $\delta = \pi$ , can be defined as  $A(M, \theta)V_{bat}$ , where  $A(M, \theta)$  is a function of the modulation index magnitude and angle, given by

$$A(M, \theta) \triangleq \frac{|\underline{V}_0^{(1)}|}{V_{bat} \left| \sin\left(\frac{\delta}{2}\right) \right|} = \frac{4}{3\pi} \sum_{i=-1}^1 \cos\left(\frac{M\pi}{2} \cos\left(\theta + i\frac{2\pi}{3}\right)\right). \quad (16)$$

While the function  $A(M, \theta)$  is mathematically dependent on both modulation index  $M$  and the modulation angle  $\theta$ , the dependence on  $\theta$  can be neglected. To demonstrate this, Fig. 7 shows the function  $A(M, \theta)$  plotted with respect to the modulation angle  $\theta$  for different values of  $M$ . Note that for every value of  $M$ , the plot is approximately a horizontal line, demonstrating the weak dependence of  $A(M, \theta)$  on  $\theta$ .

Therefore, it is possible to approximate the function  $A$ , which describes the maximum applicable voltage, given a suitable choice of carrier phase shift  $\delta$  as being dependent only on the modulation magnitude  $M$

$$A(M, \theta) \approx A(M, 0) = A'(M) = \frac{4}{3\pi} \left( \cos\left(\frac{M\pi}{2}\right) + 2\cos\left(\frac{M\pi}{4}\right) \right). \quad (17)$$

The function described in (17) is plotted in Fig. 8 and varies between  $\frac{4\sqrt{2}}{3\pi}$  and  $\frac{4}{\pi}$  for  $0 \leq M \leq 1$ . The magnitude of the zero-axis voltage can be evaluated as

$$|\underline{V}_0^{(1)}| = A'(M) \left| \sin\left(\frac{\delta}{2}\right) \right| V_{bat} \quad (18)$$

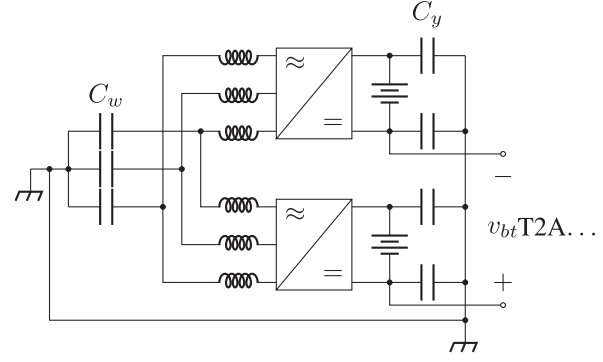


Fig. 9. Proposed traction-to-auxiliary topology in the presence of parasitic capacitances.

with  $\frac{4\sqrt{2}}{3\pi} \leq A'(M) \leq \frac{4}{\pi}$ . The function  $A'(M)$  may be taken into consideration when designing the system, to ensure the system can meet the power specifications even under the hardest power transfer scenario, i.e., when  $M = 1$ .

As a result of motor behavior, the modulation index  $M$  tends to increase approximately proportionally to the machine speed within the maximum torque per ampere operating region. As a consequence, to deliver a constant LV battery charging power, the system is expected to require a somewhat higher value of  $\delta$  at higher drive speeds than what is required at lower speeds.

### C. Filtering

The rectified sinusoidal current into the LV auxiliary battery can have a significant double switching frequency harmonic. To address this component, a CL low-pass filter can be placed after the rectifier stage, as seen in Fig. 4. By design, the current waveform's high frequency can help reduce the filter cost, allowing for the use of an air-core inductor, thus significantly reducing the filter weight. Such a filter is used in Section IV.

### D. Effects of Parasitic Capacitances

The derivations made in this section assume no parasitic capacitances. Nonetheless, in practical applications, such capacitances exist. Two such particularly important effects are the motor capacitances and the dc-link y-capacitances.

Both parasitic effects are shown schematically in Fig. 9. The y-capacitances from the dc-link to the chassis are labeled  $C_y$ , whereas the capacitances from the stator windings to the machine chassis are labeled  $C_w$ .

The effect of winding-to-chassis capacitance  $C_w$  is to allow leakage current through the stator chassis, part of which takes the form of ball bearing currents, and can decrease motor lifetime. The first harmonic approximation of the total current through the combined winding-to-chassis capacitance  $C_w$  can be computed as

$$\sum I_{cw} = \frac{\frac{A'(M)}{2} \left| \cos\left(\frac{\delta}{2}\right) \right| V_{bat}}{j\omega_{sw}(3C_w + 4C_y) + j\omega_{sw} \frac{L_s}{12}}. \quad (19)$$

Note that the voltage driving current through the machine parasitic capacitances,  $\frac{A'(M)}{2} \left| \cos\left(\frac{\delta}{2}\right) \right| V_{bat}$ , is always less than, or

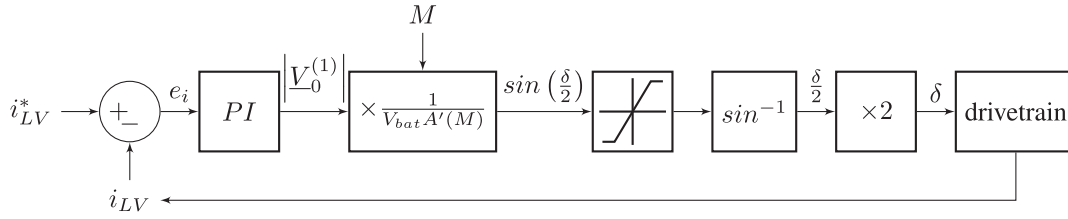


Fig. 10. Proposed control system with a PI compensator determining the voltage magnitude  $|V_0^{(1)}|$ .

equal to, the voltage driving the same currents in a conventional three-phase system, which can be shown to be  $\frac{A'(M)}{2}V_{bat}$ . Therefore, while not exploring the full cancellation afforded by six-phase systems, the proposed T2A implementation produces better or equal ball bearing current profile compared to conventional drives. As a result, the extent of ball bearing currents is out of the scope of this article.

The effect of  $C_y$  is to decrease the total voltage that is applicable to the T2A system. To achieve a power transfer  $P$ , it is required that

$$A'(M)V_{bat} > \alpha V_{LV} \left( \frac{4}{\pi} \right) G_1 G_2 \quad (20)$$

at all times, where

$$G_1 = \left| \frac{\left( \frac{1}{j\omega_{sw}C_y} \right) \parallel \left( \frac{1}{j\omega_{sw}C_r} + j\omega_{sw}L_{tr} + R_{eq} \right)}{\left( j\omega_{sw} \frac{L_s}{3} \right) + \left( \frac{1}{j\omega_{sw}C_y} \right) \parallel \left( \frac{1}{j\omega_{sw}C_r} + j\omega_{sw}L_{tr} + R_{eq} \right)} \right|, \quad (21)$$

$$G_2 = \left| \frac{R_{eq}}{\frac{1}{j\omega_{sw}C_r} + j\omega_{sw}L_{tr} + R_{eq}} \right| \quad (22)$$

and the equivalent resistive representation of the rectifier stage, referred to as the HV side, is given by

$$R_{eq} = \frac{8\alpha^2 V_{LV}^2}{\pi^2 P}. \quad (23)$$

For the experimental setup, both sets of parasitic capacitance effects, however, can be neglected during the proposed system analysis. However, in practical applications, these capacitances can be larger and may, in some cases, need to be considered. The operation shown in Section V demonstrates that  $C_y$  is sufficiently small to allow current through the T2A branch.

### III. CONTROL SYSTEM

As mentioned in Section II, the auxiliary LV battery charger operates regardless of whether the car is driving or at a standstill. As such, the T2A control system must operate without disturbing the drive control or motor torque production. The T2A control system may take variables from the driving control into consideration. The modulation index  $M$  is particularly relevant, as it has some effect on the amplitude of the applied voltage, as shown in (17) and (18).

The proposed control paradigm, shown in Fig. 4, consists of a compensator that determines the voltage magnitude  $|V_0^{(1)}|$  required by the T2A system to eliminate the current tracking

error  $e_i$ . Considering the modulation index  $M$ , the system determines the value of  $\sin(\frac{\delta}{2})$  required to synthesize such a voltage. Before the sine inverse block, a limiter saturates the input to be between  $-1$  and  $1$ , ensuring the output is defined in  $\mathbb{R}$ . Finally, the phase-shift  $\delta$  is sent to the PWM modulator in the drivetrain. Alternatively, the controller can be implemented solely with a saturable PI controller if high-speed transient performance is not required.

#### A. Compensator Design

The compensator design can be conducted considering a worst-case scenario for stability. While the transfer-function relating  $i_{LV}$  with the magnitude of the input voltage  $|V_0^{(1)}|$  is complex, it can be simplified as  $\frac{\alpha}{R}$ , where  $R$  is the series combination of the equivalent rectifier resistance and the loop resistance. In the worst-case scenario, this function is bounded by the ratio between the transformer ratio  $\alpha$  and the loop resistance, considering windings, connections, semiconductors, and other components. This approximation is only valid for closed-loop system bandwidths much lower than the switching frequency.

As a practical heuristic, for this system, a PI controller with transfer function

$$PI(s) = K \left( 1 + \frac{a}{s} \right) \quad (24)$$

can be used, where we have the following:

- 1)  $K \leq \frac{V_{bat}}{i_{LV}^{\max}}$ , with  $i_{LV}^{\max}$  representing the maximum current output of the T2A system;
- 2)  $a \approx \frac{2\pi f_{sw}}{100}$ .

These conditions simultaneously

- 1) prevent controller saturation during large transients;
- 2) result in a controller bandwidth of approximately 100 times slower than the switching frequency, which is typically fast enough for the T2A system's requirements but is slow enough so that the resistive approximation is valid.

### IV. SIMULATIONS

Simulations are conducted to verify the system's operation. In the results presented in this section, conventional techniques are used to control the driving operation and ensure the system follows a reference speed. The speed control system and its architecture and design are sufficiently discussed in the literature and therefore not covered in this article. The T2A control described in Section III ensures the proper functionality of the LV battery charging stage. This analysis aims to show that the T2A operation does not affect the driving control system.

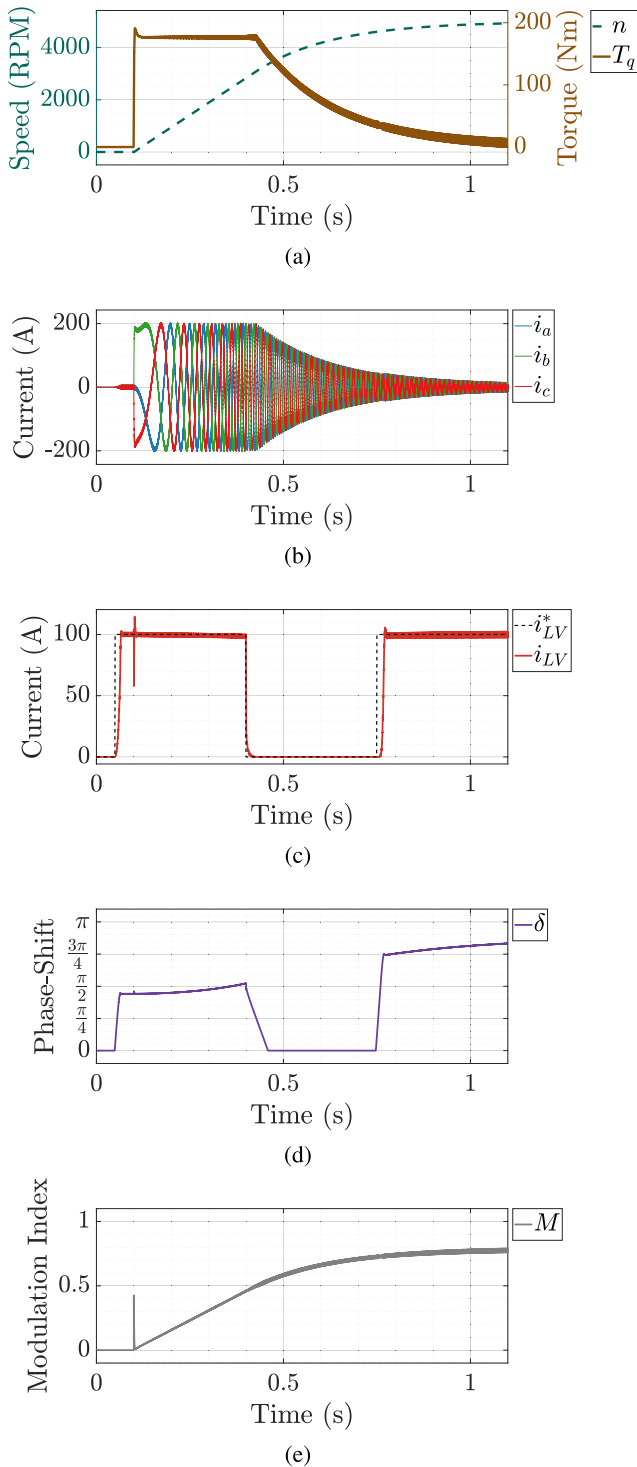


Fig. 11. Simulation results of T2A operation during acceleration of drivetrain. (a) Machine speed and torque. (b) Machine phase current waveforms. (c) Current reference and actual current into the auxiliary battery. (d) Carrier phase-shift between top and bottom inverters. (e) Dual inverter PWM modulation index.

The simulations in this section use the circuit represented in Fig. 4, driving a permanent magnet synchronous machine.

The simulation parameters are shown in Table I. The voltage ratings are selected to represent typical voltages present in a commercial EV. The motor parameters are selected to represent the machine HSM-60, manufactured by TM4, used in Section V

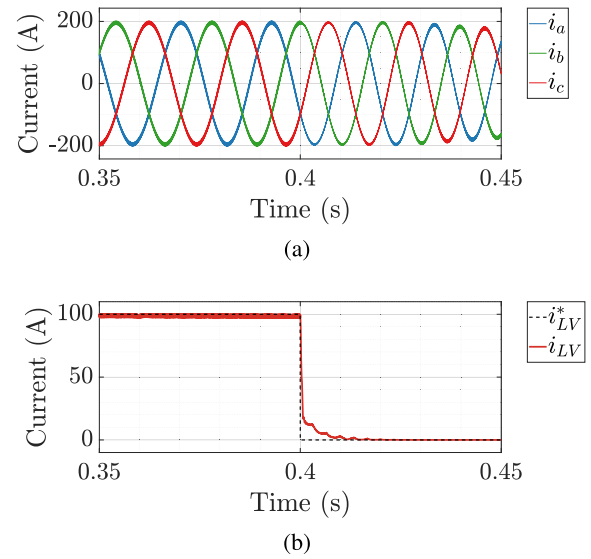


Fig. 12. Simulation results zoomed in on 100 to 0 A transient change of T2A reference current. (a) Machine phase currents. (b) T2A output current.

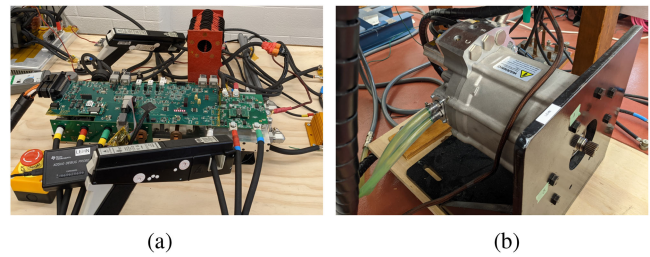


Fig. 13. Preexisting drivetrain parts. (a) Drivetrain. (b) PMSM.

TABLE I  
PARAMETERS USED IN SIMULATION

Description	Symbol	Value
System		
Batteries' voltage	$V_{\text{bat}}$	400 V
Auxiliary voltage	$v_{\text{LV}}$	12 V
Switching frequency	$f_{\text{sw}}$	10 kHz
Machine		
0-Seq. inductance	$L_S$	0.53 mH
$q$ -axis inductance	$L_q$	0.94 mH
$d$ -axis inductance	$L_d$	0.73 mH
Series resistance	$R_S$	45 m $\Omega$
Pole pairs	$p/2$	10
Flux linkage	$\lambda_S$	0.127 Wb
Rated current (rms)	$I_{\text{max}}$	200 A
T2A		
Transformer inductance	$L_{\text{tr}}$	700 $\mu\text{H}$
Compensation capacitor	$C_r$	280 nF
Turns ratio	$\alpha$	20 V/V
Filter capacitance	$C_f$	4 mF
Filter inductance	$L_f$	5.37 $\mu\text{H}$

and shown in Fig. 13(b). The T2A transformer and compensation capacitor  $C_r$  are selected to ensure resonance, as prescribed in (5), while filter components,  $C_f$  and  $L_f$ , are selected based on available laboratory stock components that are employed for experimental verification.

The simulation test, whose results are shown in Fig. 11, consists of accelerating the drive system from rest to 5000 r/min at time  $t = 0.1$  s. This high speed value was set in simulation to ensure a high modulation index in the inverters, making explicit the dependence of  $|V_0^{(1)}|$  on  $M$ , described in (17) and (18) and illustrated in Fig. 8. In the simulation, the vehicle inertia and friction have been set to low values, while the torque controller is designed to provide a fast response (in the order of 1-ms rise time) in an attempt to demonstrate the T2A operation even in the presence of transients significantly more severe than what can be expected in practical applications.

In simulation, the LV battery current reference is initialized to 0. At  $t = 0.05$  s, before the acceleration takes place, the reference is set to  $i_{LV}^* = 100$  A. As a result, the T2A system is operating while the acceleration transient is applied, showcasing the effect of disturbance introduced by the drive controller onto the T2A system. At time  $t = 0.4$  s, the reference is set back to 0, and at time  $t = 0.75$  s, it is raised to 100 A once more, showcasing the effects of disturbances introduced by the T2A transients onto the driving system. The simulation results are shown in Fig. 11.

Fig. 11(a) shows the speed and torque responses of the system to the transient described above. As the speed reference step is applied, the drive controller increases the torque to its maximum value, determined by the maximum allowable machine winding current. As a result, the speed increases, converging to the reference value of 5000 r/min. To achieve this behavior, an inner control loop increases the stator currents, as shown in Fig. 11(b). The system's speed, torque, and stator winding currents are typical for permanent magnet synchronous motor (PMSM) drives. This result demonstrates that the integrated T2A functionality does not interfere with drive operation.

The T2A controller has a variable reference for LV battery current as described above. The reference current is shown in Fig. 11(c), as well as the actual current output to the LV battery. The control scheme shown in Fig. 10 adequately tracks the reference current. The T2A system controls the carrier phase-shift between inverters  $\delta$ , as shown in Fig. 11(d). At  $t = 0.05$  s, as the T2A reference output current increases, the value of  $\delta$  requested by the control system increases commensurately, tracking the current command. Despite the large T2A transient, no disturbance is noted in the speed or torque signals shown in Fig. 11(a), highlighting the fact that T2A operation does not interfere with driving functionality.

At  $t = 0.1$  s, as the acceleration transient is applied, in an attempt to quickly raise the torque, the drive control applies a large  $M$  transient, seen as a spike in Fig. 11(e). This sudden variation in  $M$  imposes a transient onto the T2A system, as per (17). Even in this extreme circumstance, which is more severe than

expected in practical applications, the T2A controller quickly reestablishes tracking. At  $t = 0.4$  s, as the current reference is set to zero, the phase-shift decreases to zero, thereby tracking the current reference.

As the speed continuously increases, so does the modulation index  $M$ , as shown in Fig. 11(e). This effect is typical and expected in drive systems. The modulation index variation changes the required value of  $\delta$  for a given T2A output power. In the simulation result, this effect can be seen best between  $t = 0.25$  s and  $t = 0.4$  s. The rapid increase in speed causes a rapid increase in modulation index. To maintain the same output power, the controller increases the phase shift, according to (15).

Near the end of the simulation, as the machine speed approaches nominal values and modulation index approaches unity, a significantly larger  $\delta$  is required to output the same current level. This effect can be seen in Fig. 11(d), as the value of  $\delta$  is significantly greater near the end of the simulation period, despite the identical current reference  $i_{LV}^*$ .

To examine the impact of T2A transients on driving currents, Fig. 12(a) shows the machine phase currents during the step transient in reference current output from the T2A shown in Fig. 12(b). The transient happening around 0.4 s is chosen for this demonstration as the phase current magnitude is approximately constant when the change occurs. Since the magnitude of the currents resulting from driving operation are several orders of magnitude larger than those resulting from T2A operation, no appreciable change is seen due to the transient. This result is a consequence of the orders of magnitude difference in power ratings, making T2A imposed currents negligible to the drivetrain.

## V. EXPERIMENTAL VERIFICATION

An experimental prototype, as shown in Fig. 13(a), was designed to verify the analytical claims and validate the simulation results. This section covers the design calculations pertaining to the construction of the experimental setup and the operation thereof. The circuitry can be decomposed into two parts: pre-existing drivetrain parts and added circuitry. The preexisting drivetrain parts are shown in Fig. 13. The added circuitry is shown in Fig. 14. Note that the T2A additional circuitry is simple enough to be designed with lab available parts, including the aircore inductor, and is not optimized for power density. All parameters used in experimental verification are identical to what is described in Table I unless otherwise specified.

### A. Transformer Design

To enable the drivetrain integrated T2A, the transformer depicted in Fig. 4 must be designed. The transformation ratio is chosen such that the system can operate for all values of  $M$ . The design, therefore, considers the case where  $M$  is approximately 1 and  $A'(M) \approx \frac{4\sqrt{2}}{3\pi}$ , as this case produces the smallest value of  $A'(M)$ . In the tests conducted in this work, the HV battery voltage is 400 V and the LV battery voltage is 12 V, as shown in Table I. Therefore, the transformation ratio, defined here as the

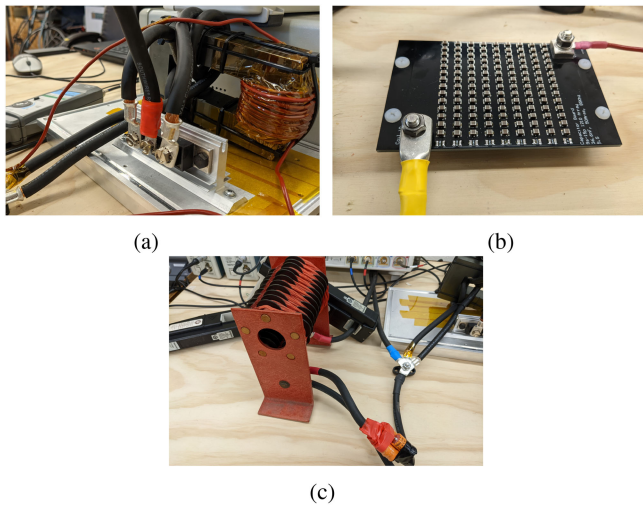


Fig. 14. Added circuitry for T2A functionality. (a) Transformer and rectifier. (b) Compensation capacitor  $C_r$ . (c) CL filter with electrolytic capacitor and aircore inductor.

TABLE II  
EXPERIMENTALLY MEASURED TRANSFORMER PARAMETERS, AS SEEN ON THE HV SIDE

Parameter	Variable	Value
Leakage inductance	$L_{tr}$	698 $\mu\text{H}$
Series resistance	$R_s$	658 $\text{m}\Omega$
Magnetizing inductance	$L_m$	11.32 $\text{mH}$
Parallel resistance	$R_m$	144 $\text{k}\Omega$

ratio between the turns on the HV side and on the LV side

$$\alpha = \frac{4\sqrt{2} V_{bat}}{3\pi V_{LV}} \approx 20. \quad (25)$$

In practical applications, a lower turns ratio value might be desired to accommodate different HV and LV batteries' state of charge.

The transformer is designed to have 40 turns on the HV side and two turns on each half winding of the LV side, as shown in Fig. 14(a). The transformer parameters are measured and shown in Table II.

### B. Compensation Capacitor

Once the transformer parameters are determined, the leakage inductance can be used to design the compensation capacitor, as described in (5). Given the transformer parameters, a capacitance of approximately 280 nF is required. The capacitor is implemented using a matrix of surface mount ceramic capacitors to observe the current and voltage stress on the component. The capacitor is shown in Fig. 14(b).

### C. Power Electronics, Machine, and Power Supplies

The control algorithm is implemented in an F28379D digital signal processor (DSP), by Texas Instruments. Two HP1 three-phase insulated-gate bipolar transistor modules, by Infineon,

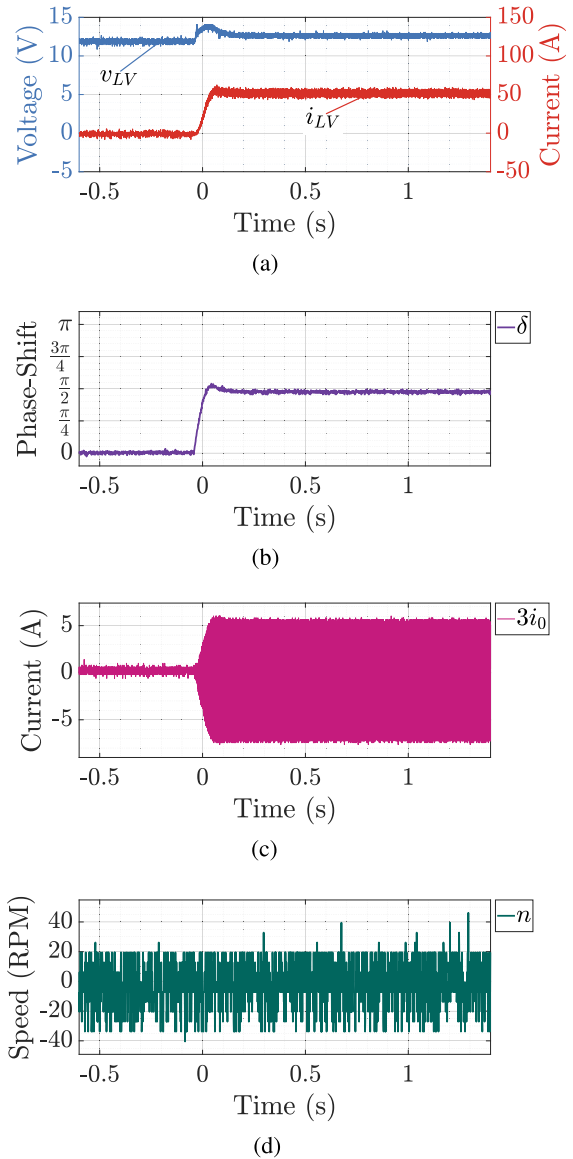


Fig. 15. Experimentally measured waveforms during T2A output current step from 0 to 50 A at standstill. (a) T2A voltage and current output. (b) Phase-shift imposed by the controller, outputted via DAC. (c) Current at the primary winding of the T2A transformer. (d) Speed read by DSP outputted via DAC.

are used to implement the drivetrain prototype, as shown in Fig. 13(a). A 110 kW PMSM HSM-60 machine, by TM4, is driven, as shown in Fig. 13(b). The motor is operated with a conventional speed controller, comprising an outer-loop speed control and an inner-loop current control system. Two EA-PSB power supplies are used to emulate the 400 V batteries. A dc e-load model 63207, by Chroma, is used to emulate the 12 V battery as a constant voltage load. The parasitic capacitances  $C_y$  and  $C_w$  are measured using an impedance analyzer and determined to be, respectively, 6 and 2.4 nF.

### D. Results

The prototype shown in Fig. 14 is used to conduct three experiments.

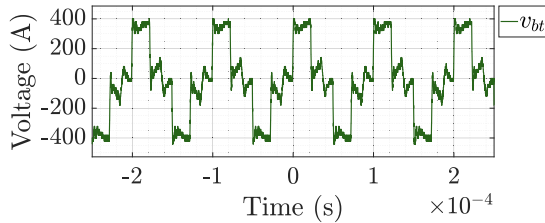


Fig. 16. Voltage between negative terminal of both batteries  $v_{bt}$  during steady-state operation. T2A output current at 50 A.

- 1) The system is subject to a step in T2A current output reference from 0 to 50 A to demonstrate T2A control transient performance. This experiment also demonstrates that T2A transient does not affect the motor drive system.
- 2) The T2A system is operated at 100 A, demonstrating high power transfer capability and providing a visual examination of component stress.
- 3) With T2A system outputting 50 A, a step-in motor speed reference is applied to the drive controller, from 0 to 1500 r/min. This experiment demonstrates that drive control operates normally under T2A power transfer and that practical drive transient does not appreciably affect T2A operation.

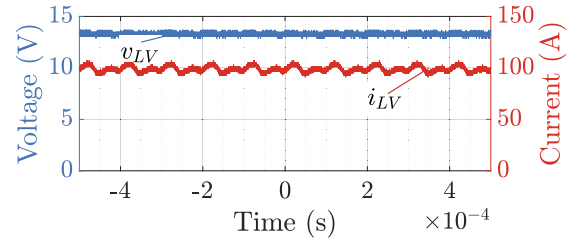
For the first experiment, the system is initially conducting 0 A at the output of the T2A system. Around time  $t = 0$  s, the reference output current is set to  $i_{LV}^* = 50$  A. The control system shown conceptually in Fig. 10 enforces the reference tracking and the output current rises to  $i_{LV} = 50$  A, as shown in Fig. 15(a).

To increase the T2a output current  $i_{LV}$ , the controller increases the magnitude of the zero-axis voltage by imposing a carrier phase-shift  $\delta$  between inverters. The  $\delta$  requested by the controller is extracted from the DSP using a digital-to-analog converter (DAC) and is shown in Fig. 15(b). As a result, the transformer's HV winding switching frequency current component magnitude increases. This effect can be observed in Fig. 15(c). The voltage  $V_{LV}$  is controlled by the e-load, which maintains the voltage approximately at 12 V.

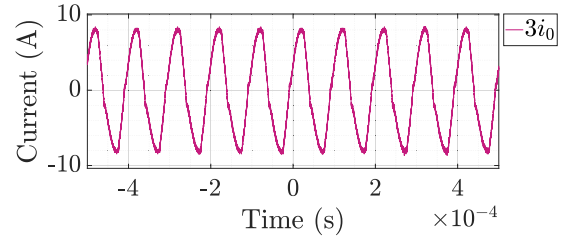
The speed, read by the DSP from the machine's built-in resolver, is also outputted via DAC. The resulting experimental speed measurement is shown in Fig. 15(d). No appreciable disturbance is seen in the speed measurement, and no movement is observed in the physical motor during the test, despite no load on the rotor, as shown in Fig. 13(b). This result suggests that the T2A step does not impose any torque disturbance on the drive system.

When the current settles around 50 A, the voltages between the negative terminal of bottom and top batteries  $v_{bt}$  is measured. This is the voltage applied to the series combination of  $C_r$  and primary side of the transformer. The resulting waveform is shown in Fig. 16 and has a dominant sinusoidal component at the switching frequency. Higher order harmonics of this voltage are filtered by the transformer inductance and do not cause significant current.

For the second test, the T2A system is kept in steady-state with output current reference  $i_{LV}^* = 100$  A, while the drive is at a standstill. The T2A output voltage and current are shown



(a)



(b)

Fig. 17. Experimentally measured waveforms during steady-state T2A operation with  $i_{LV}^* = 100$  A. (a) T2A voltage and current output. (b) Current at the primary winding of the T2A transformer.

in Fig. 17(a). The current through the HV windings of the transformer is shown in Fig. 17(b) and can be seen to be approximately sinusoidal and have a frequency of 10 kHz, i.e., the switching frequency  $f_{sw}$ , as predicted by the theory laid out in Section II. The peak amplitude of the current is approximately 8 A. The measured rms current imposed onto the machine phase windings is 2.84 A, which is less than 1.5% of the machine rated current 200 A.

For the third and last experiment, the T2A system is at steady-state, with  $i_{LV}^* = 50$  A. The current into the HV winding of the transformer can be observed in Fig. 18(d), and it has a similar magnitude as shown in Fig. 15(c), after the current reference step.

Starting approximately at time  $t = 0$  s, the speed reference of the drive system is ramped up, from 0 to 1500 r/min. The speed controller raises the speed throughout approximately 15 s, as shown in Fig. 18(a). To accelerate, sinusoidal currents are imposed onto the machine stator windings, with phase "a" shown in Fig. 18(b). In this test, the rotor has no load, and, as a result, the stator current required for acceleration is relatively small compared to the machine's rated current. The drive system operates regularly, regardless of the simultaneous T2A operation, which imposes zero-sequence current through the machine.

The T2A operation is undisturbed by the acceleration. In Fig. 18(c),  $V_{LV}$  and  $i_{LV}$  are shown to be constant. The current through the HV side of the T2A transformer is also undisturbed, as shown in Fig. 18(d). This rejection is achieved by designing the T2A controller with enough bandwidth to reject the modulation index variations imposed by the speed controller, as it raises the machine current magnitude in response to a change in speed reference.

As the speed increases, the modulation index  $M$  increases, decreasing the value of  $A'(M)$ , as per (17). To compensate for this effect, even a simple PI controller changes  $\delta$  to maintain the

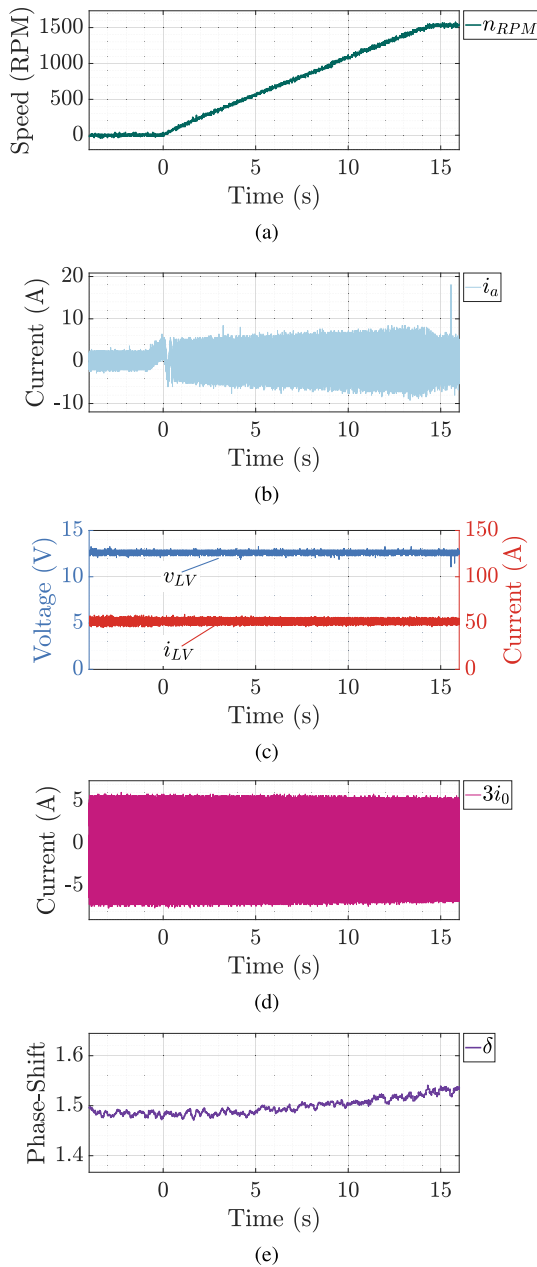


Fig. 18. Experimentally measured waveforms during steady-state T2A operation with output current reference  $i_{LV}^* = 50$  A and speed reference step from 0 to 1500 r/min. (a) Motor speed read by the DSP and outputted via DAC. (b) Machine winding current through phase “a.” (c) T2A voltage and current output. (d) Current at the primary winding of the T2A transformer. (e) Phase-shift imposed by the controller, outputted via DAC. Signal filtered by a moving average of 19 scope samples to enhance signal-to-noise ratio.

reference current output. The phase-shift is outputted via DAC, filtered using a moving average filter, and shown in Fig. 18(e). The moving average filter enhances the visualization since the change in  $\delta$  is fairly small compared to the DAC quantization and measurement noises. The measured  $\delta$ , after filtering, can be seen to increase slightly as the speed increases.

## VI. CONCLUSION

A T2A converter is proposed to feed the LV auxiliary battery charging in dual inverter EVs. The system uses multifrequency power transfer, reserving low frequencies for the drive operation and leveraging zero-sequence current at the switching frequency for T2A operation. No additional active switches are necessary to control the power transfer between the main traction and LV auxiliary batteries. Instead, a carrier phase shift is established between the top and bottom inverters of the drivetrain. As a result, at the switching frequency, zero-axis current is established and controlled through the open winding machine stator and is used for power transfer. Moreover, during simultaneous driving and charging operation, no additional switching takes place, as the switching action of the driving operation is leveraged, while the additional current imposed on the machine windings is less than 1.5% of the rated value. Therefore, the proposed scheme significantly reduces additional loss during driving mode compared to comparable APMs, which invariably require some dedicated PEIs.

An experimental 1.2 kW prototype is designed to demonstrate the proposed functionality. The converter is shown to operate undisturbed during variations in driving conditions, including acceleration transients. Similarly, transients in auxiliary current output are demonstrated not to affect the drive system.

The proposed auxiliary power supply additional circuitry consists of capacitors, an isolation transformer, and a rectifier. The reduced number of components and conversion stages make this circuit superior to previously proposed solutions both in cost and weight.

## REFERENCES

- [1] J. Asamer, A. Graser, B. Heilmann, and M. Ruthmair, “Sensitivity analysis for energy demand estimation of electric vehicles,” *Transp. Res. Part D: Transport Environ.*, vol. 46, pp. 182–199, 2016. [Online]. Available: <http://dx.doi.org/10.1016/j.trd.2016.03.017>
- [2] M. Coffman, P. Bernstein, and S. Wee, “Factors affecting EV adoption: A literature review and EV forecast for Hawaii,” *Electric Veh. Transp. Center*, vol. 37, pp. 1–36, Apr. 2015.
- [3] S. M. Hasan, M. N. Anwar, M. Teimorzadeh, and D. P. Tasky, “Features and challenges for auxiliary power module (APM) design for hybrid/electric vehicle applications,” in *Proc. IEEE Veh. Power Propulsion Conf.*, 2011, pp. 1–6.
- [4] L. Zhu, H. Bai, A. Brown, and M. McAmmond, “Two-stage vs one-stage design for a bidirectional 400 V/12 V 6 kW auxiliary power module in electric vehicles,” in *Proc. IEEE Transp. Electrific. Conf. Expo.*, 2020, pp. 1222–1226.
- [5] L. Zhu, H. K. Bai, A. Brown, and M. McAmmond, “Dynamic process analysis of a high-power bidirectional DC/DC converter for electric vehicles,” in *Proc. IEEE Energy Convers. Congr. Expo.*, 2020, pp. 864–870.
- [6] L. Zhu, H. Bai, A. Brown, and M. McAmmond, “Design a 400 V-12 v 6 kW bidirectional auxiliary power module for electric or autonomous vehicles with fast precharge dynamics and zero DC-Bias current,” *IEEE Trans. Power Electron.*, vol. 36, no. 5, pp. 5323–5335, May 2021.
- [7] R. Hou, P. Magne, B. Bilgin, and A. Emadi, “A topological evaluation of isolated DC/DC converters for auxiliary power modules in electrified vehicle applications,” in *Proc. Conf. IEEE Appl. Power Electron. Conf. Expo.*, 2015, pp. 1360–1366.
- [8] R. Hou and A. Emadi, “Evaluation of integrated active filter auxiliary power modules in electrified vehicle applications,” in *Proc. IEEE Energy Convers. Congr. Expo.*, 2015, pp. 6314–6319.
- [9] R. Muhammad, S. Kim, C. Suk, S. Choi, B. Yu, and S. Park, “Integrated planar transformer design of 3-kW auxiliary power module for electric vehicles,” in *Proc. IEEE Energy Convers. Congr. Expo.*, 2020, pp. 1239–1243.

- [10] A. M. Naradhpa, S. Kim, D. Yang, S. Choi, I. Yeo, and Y. Lee, "Power density optimization of 700 kHz GaN-Based auxiliary power module for electric vehicles," *IEEE Trans. Power Electron.*, vol. 36, no. 5, pp. 5610–5621, May 2021.
- [11] H. Moradisizkoohi, N. Elsayad, and O. A. Mohammed, "Experimental demonstration of a modular, quasi-resonant bidirectional DC-DC converter using GaN switches for electric vehicles," *IEEE Trans. Ind. Appl.*, vol. 55, no. 6, pp. 7787–7803, Nov./Dec. 2019.
- [12] G. Yu and S. Choi, "Auxiliary power module - integrated EV charger with extended ZVS range," in *Proc. IEEE Energy Convers. Congr. Expo.*, 2020, pp. 628–632.
- [13] R. Hou and A. Emadi, "Dual active bridge-based full-integrated active filter auxiliary power module for electrified vehicle applications with single-phase onboard chargers," in *Proc. IEEE Appl. Power Electron. Conf. Expo.*, 2016, pp. 1300–1306.
- [14] R. Hou and A. Emadi, "A primary full-integrated active filter auxiliary power module in electrified vehicles with single-phase onboard chargers," *IEEE Trans. Power Electron.*, vol. 32, no. 11, pp. 8393–8405, Nov. 2017.
- [15] R. Hou and A. Emadi, "Applied integrated active filter auxiliary power module for electrified vehicles with single-phase onboard chargers," *IEEE Trans. Power Electron.*, vol. 32, no. 11, pp. 8393–8405, Mar. 2017.
- [16] M. Evzelman, M. M. Ur Rehman, K. Hathaway, R. Zane, D. Costinett, and D. Maksimovic, "Active balancing system for electric vehicles with incorporated low-voltage bus," *IEEE Trans. Power Electron.*, vol. 31, no. 11, pp. 7887–7895, Nov. 2016.
- [17] W. Wang and M. Preindl, "Dual cell links for battery-balancing auxiliary power modules: A cost-effective increase of accessible pack capacity," *IEEE Trans. Ind. Appl.*, vol. 56, no. 2, pp. 1752–1765, Mar./Apr. 2020.
- [18] Z. Gong *et al.*, "EV BMS with time-shared isolated converters for active balancing and auxiliary bus regulation," in *Proc. Int. Power Electron. Conf.*, 2018, pp. 267–274.
- [19] M. Preindl, "A battery balancing auxiliary power module with predictive control for electrified transportation," *IEEE Trans. Ind. Electron.*, vol. 65, no. 8, pp. 6552–6559, Aug. 2018.
- [20] A. Khaligh and M. Dantonio, "Global trends in high-power on-board chargers for electric vehicles," *IEEE Trans. Veh. Technol.*, vol. 68, no. 4, pp. 3306–3324, Apr. 2019.
- [21] L. Zhu, H. Bai, A. Brown, and L. Keuck, "A current-fed three-port DC/DC converter for integration of on-board charger and auxiliary power module in electric vehicles," in *Proc. IEEE Appl. Power Electron. Conf. Expo.*, 2021, pp. 577–582.
- [22] Y. Tang, J. Lu, B. Wu, S. Zou, W. Ding, and A. Khaligh, "An integrated dual-output isolated converter for plug-in electric vehicles," *IEEE Trans. Veh. Technol.*, vol. 67, no. 2, pp. 966–976, Feb. 2018.
- [23] B. Farhangi and H. A. Toliyat, "Modeling and analyzing multiport isolation transformer capacitive components for onboard vehicular power conditioners," *IEEE Trans. Ind. Electron.*, vol. 62, no. 5, pp. 3134–3142, May 2015.
- [24] J. G. Pinto, V. Monteiro, H. Gonçalves, and J. L. Afonso, "Onboard reconfigurable battery charger for electric vehicles with traction-to-auxiliary mode," *IEEE Trans. Veh. Technol.*, vol. 63, no. 3, pp. 1104–1116, Mar. 2014.
- [25] S. Kim and F. S. Kang, "Multifunctional onboard battery charger for plug-in electric vehicles," *IEEE Trans. Ind. Electron.*, vol. 62, no. 6, pp. 3460–3472, Jun. 2015.
- [26] S. Semsar, T. Soong, and P. W. Lehn, "On-board single-phase integrated electric vehicle charger with V2G functionality," *IEEE Trans. Power Electron.*, vol. 35, no. 11, pp. 12072–12084, Nov. 2020.
- [27] S. Semsar, T. Soong, and P. W. Lehn, "Integrated single-phase electric vehicle charging using a dual-inverter drive," in *Proc. IEEE Trans. Electrific. Conf. Expo.*, 2018, pp. 320–325.
- [28] B. A. Welchko, T. M. Jahns, and T. A. Lipo, "Short-circuit fault mitigation methods for interior PM synchronous machine drives using six-leg inverters brian," in *Proc. 35th Annu. IEEE Power Electron. Specialists Conf.*, 2004, pp. 2133–2139.
- [29] R. Menon, S. S. Williamson, N. A. Azeez, and A. H. Kadam, "A fault tolerant modulation strategy for dual inverter traction drives," in *Proc. IEEE Energy Convers. Congr. Expo.*, 2019, pp. 5856–5861.
- [30] M. Pathmanathan, C. Viana, S. Semsar, and P. Lehn, "Open-phase fault tolerant driving operation of dual-inverter-based traction drive," *IET Electric Power Appl.*, vol. 15, no. 7, pp. 873–889, 2021.
- [31] J. Kim, J. Jung, and K. Nam, "Dual-inverter control strategy for high-speed operation of EV induction motors," *IEEE Trans. Ind. Electron.*, vol. 51, no. 2, pp. 312–320, Apr. 2004.
- [32] S. Singh, C. Perera, G. J. Kish, and J. Salmon, "PWM control of a dual inverter drive using a floating capacitor inverter," in *Proc. IEEE 20th Workshop Control Model. Power Electron.*, 2019, pp. 1–8.
- [33] K. A. Corzine, S. D. Sudhoff, and C. Whitcomb, "Performance characteristics of a cascaded two-level converter," *IEEE Trans. Energy Convers.*, vol. 14, no. 3, pp. 433–439, Sep. 1999.
- [34] R. Shi, S. Semsar, and P. W. Lehn, "Constant current fast charging of electric vehicles via a DC grid using a dual-inverter drive," *IEEE Trans. Ind. Electron.*, vol. 64, no. 9, pp. 6940–6949, Sep. 2017.
- [35] C. Viana and P. W. Lehn, "A drivetrain integrated DC fast charger with buck and boost functionality and simultaneous drive/charge capability," *IEEE Trans. Transport. Electrific.*, vol. 5, no. 4, pp. 903–911, Dec. 2019.
- [36] A. D. Brovont and S. D. Pekarek, "Derivation and application of equivalent circuits to model common-mode current in microgrids," *IEEE Trans. Emerg. Sel. Topics Power Electron.*, vol. 5, no. 1, pp. 297–308, Mar. 2017.
- [37] E. Clarke, "Problems solved by modified symmetrical components," *Gen. Electric Rev.*, vol. 41, no. 11 and 12, pp. 488–449, 1938.
- [38] C. J. O'Rourke, M. M. Qasim, M. R. Overlin, and J. L. Kirtley, "A geometric interpretation of reference frames and transformations: DQ0, Clarke, and Park," *IEEE Trans. Energy Convers.*, vol. 34, no. 4, pp. 2070–2083, Dec. 2019.



**Caniggia Castro Diniz Vian** (Student Member, IEEE) received the B.A.Sc. degree in electrical engineering from the Federal University of Rio Grande do Norte, Natal, Brazil, in 2017.

He is currently working toward the Ph.D. degree in electrical engineering with the University of Toronto, Toronto, Canada.

His current research interests include integrated implementation of power EV conversion functionalities and standard compliance.



**Mehanathan Pathmanathan** received the B.E. (Hons.) and Ph.D. degrees in electrical and electronic engineering from The University of Adelaide, Adelaide, Australia, in 2007 and 2012, respectively.

From 2012 to 2018, he was a Research Engineer with the Machines and Drives Team, ABB Corporate Research, Sweden. Since 2018, he has been a Research Associate with the University of Toronto, Toronto, ON, Canada.

His current research interests include electric vehicle powertrains, medium voltage drives, and wireless

power transfer.



**Peter W. Lehn** received the B.Sc. and M.Sc. degrees in electrical engineering from the University of Manitoba, Winnipeg, MN, Canada, in 1990 and 1992, respectively, and the Ph.D. degree from the University of Toronto, Toronto, ON, Canada, in 1999 in the area of Modeling and Control of Power Electronic Converters.

In 1999, he joined the University of Toronto, as a Faculty. He spent six months as a Visiting Professor at the University of Erlangen-Nuremberg, Erlangen, Germany, in 2001. His current research interests include HVDC technologies, grid integration of storage and renewables, power electronics for electric vehicles, and theoretical analysis of power electronic systems.

Dr. Lehn has been an Editor of IEEE TRANSACTIONS ON ENERGY CONVERSION from 2013 to 2019.